Available online at www.sciencedirect.com

ScienceDirect

journal homepage: www.elsevier.com/locate/he

Multi-objective optimization of channel structure for a proton exchange membrane water electrolysis cell

Yubin Zhuang, Pan Cui, Rui Long, Wei Liu, Zhichun Liu *

School of Energy and Power Engineering, Huazhong University of Science and Technology, Wuhan 430074, China

HIGHLIGHTS

- PEMEC channel height influences the gas fraction, voltage, and pressure drop.
- The channel width has a stronger influence on voltage.
- GA was used to optimize PEMEC channel structure with two objectives.
- The optimized model was characterized by a decrease in pressure drop of 34.97%.

ARTICLE INFO

Article history:
Received 1 April 2023
Received in revised form
5 July 2023
Accepted 2 August 2023
Available online 19 August 2023

Keywords:
Proton exchange membrane water electrolysis cell
Flow field
Genetic algorithm
Optimization

ABSTRACT

The flow field dominates the process of mass transport and distribution inside the proton exchange membrane water electrolysis cell (PEMEC). Initially, a three-dimensional and non-isothermal PEMEC channel model was estimated to investigate the impact of channel height and width. Based on these results, a complete PEMEC model with a parallel flow-field pattern was developed, and the channel heights and widths of the model were optimized using a genetic algorithm (GA). Compared to the original model, the optimized model decreased the pressure drop by 34.97% at a lower voltage. In addition, because of the optimized flow-field pattern, the optimized model improves the current density on the proton exchange membrane as well as the gas holdup situation in a partial position in the cathode gas diffusion layer.

1. Introduction

In the last century, the global energy demand has continuously increased [1]. Simultaneously, fossil fuel reserves have decreased sharply due to high demand. As fossil fuel-based energy sources promote environmental disruption, to defend against environmental crisis, several types of renewable energy, such as wind, solar, and tidal energy, are used to replace traditional energy sources [2]. However, a significant shortcoming of most renewable energy sources is that the power produced is periodic. Consequently, it is difficult to connect these power sources to the grid [3]. One practical method to address this problem is the combination of renewable energy with hydrogen technology, i.e., establishing a hydrogen energy system and storing and using green power in the form of hydrogen [4]. Nevertheless, to generate hydrogen, it is necessary to develop a method for producing hydrogen efficiently

* *Corresponding author.*
E-mail address: zcliu@hust.edu.cn (Z. Liu).
https://doi.org/10.1016/j.ijhydene.2023.08.026

Nomenclature

a	specific surface area (m^{-1})
A	current (A)
C	molar concentration (mol m^{-3})
Cp	specific heat capacity (J kg^{-1} K^{-1})
d	thickness (mm)
D	mass diffusivity (m^2 s^{-1})
F	faraday constant
H	channel height (mm)
i_v	volumetric current density (A m^{-3})
k	thermal conductivity (W m^{-1} K^{-1})
K	permeability (m^2)
M	molecular weight (mol kg^{-1})
N	mass flow rate (kg s^{-1})
p	pressure (Pa)
P	power (W)
Q	volumetric flowrate (ml min^{-1})
R	resistance (Ω)
R_u	universal gas constant (J mol^{-1} K^{-1})
S	source item
T	temperature (K)
u	velocity (m s^{-1})
V	voltage (V)
V_{eq}	reversible voltage (V)
W	channel width (mm)

Greek letters

α	charge transfer coefficient
ε	porosity
η	over potential (V)
η_{en}	efficiency (%)
θ	covering coefficient
λ	membrane water content
μ	viscosity (Pa s^{-1})
ρ	density (kg m^{-3})
σ	conductivity (S m^{-1})
φ	potential (V)
ϕ	volume fraction
LHV	low heating value (J kg^{-1})

Subscripts and Superscripts

0	reference
a	anode
act	active
c	cathode
diff	diffusion
e	electrolyte
eff	effective
fm	fluid mixtures
g	gas
i	species "i"
ij	species "i" to species "j"
in	inlet
l	liquid
m	membrane or mass
op	operation
s	electron
v	momentum
x	component "x"

and stably. Considering the need to lower carbon emissions, water electrolysis may be one of the most feasible methods for hydrogen production in the future [5,6]. There are three main water electrolysis technologies: alkaline, proton exchange membrane, and solid oxide [7]. Among these methods, proton exchange membrane water electrolysis is associated with a higher current density, response speed, and efficiency [8], thus showing outstanding adaptability to renewable energy [9].

Previously, models were developed to simulate the effect of operation parameters on the proton exchange membrane water electrolysis cell (PEMEC). Medina et al. [10] developed a PEMEC model by analyzing water transported through a membrane under different operating conditions. Zhang et al. [11] established a PEMEC system and derived efficiency curves that varied with the electric current density. Chandesris et al. [12] built a one-dimensional PEMEC model to study the influence of temperature and current density on membrane degradation. Ojong et al. [13] discussed mass transport processes in terms of operation parameters using a PEMEC model. A simplified PEMEC model was presented by Liso et al. [14] to investigate the impact of current density on the performance. Toghyani et al. [15] developed a thermodynamic model for PEMEC and applied the Taguchi method to optimize operating parameters. Correa et al. [16] developed a PEMEC model under high pressure and analyzed the influence of pressure on the cathodic activation overpotential term. Upadhyay et al. [17] developed a single-channel-based computational field dynamics (CFD) model to analyze the influence of operational parameters. Xiao et al. [18] constructed a PEMEC model and investigated the distribution of liquid saturation and gas components inside the diffusion layer according to the operating conditions. Zhao et al. [19] established a high-temperature PEMEC model to determine the impact of the operational parameters on the performance. Salari et al. [20] used a model of a coupled photovoltaic thermal-PEMEC system to investigate the effect of various operating parameters. A transient PEMEC stack model was developed by Zhang et al. [21] to investigate the dynamic response of the performance.

The flow field plays an important role in PEMEC, dominating the processes of mass transport and distribution inside the cell. Several researchers have used CFD simulations to provide advice on design modifications and optimized parameters. Ruiz et al. [22] developed a high-temperature PEMEC model to study the effects of different channel geometries. Tijani et al. [23] evaluated the hydrodynamic properties of three flow plate designs, and the results indicated that parallel flow channel designs were the most encouraging. Toghyani et al. [24] presented a comparison between 5 PEMEC models with different flow-field patterns and concluded that the 2-path pattern was the best flow-field pattern among the simulated models. They also investigated a PEMEC model using a metal foam flow distributor [25]. Nafchi et al. [26] used a mathematical model to investigate the effects of structural parameters on PEMEC performance and observed that

reducing the height and width of the channel could decrease the voltage. Olesen et al. [27] developed a full-scale PEM electrolysis cell model with three different circular, interdigitated anode flow fields to study cells operating at high current densities. Zhang et al. [28] created a PEMEC model and discovered that a shallower, wider channel could improve water transmission, whereas increasing the channel width may cause incremental electrical losses. Jia et al. [29] investigated oxygen production in a manifold PEMEC and showed that increasing the number of channels leads to a more uniform pressure distribution inside the manifold. Chen et al. [30] built a PEMEC model with a new interdigitated jet–hole flow field and explored its operational modes and structural parameters. Wu et al. [31] integrated the detailed channel two-phase flow into the PEMEC model and found that if the oxygen in the anode channel was neglected, the simulation results of the parallel and serpentine flow fields would be almost the same. Then, they proposed a novel structured mesh channel to enhance the oxygen discharge capacity of PEMEC [32].

For parameter optimization, the genetic algorithm (GA) has been used for some time to improve fuel cells. Mert et al. [33] conducted a multi-objective optimization of a vehicular PEMFC system via a GA to maximize the power output, energy, and exergy efficiencies, and minimize cost generation. Ohenoja et al. [34] proved that the GA is one of the best methods for estimating the parameters in electrochemical models of fuel cells. Chen et al. [35] realized a Function Neural Network-GA metamodeling optimal approach to promote the performance of the design factors of PEMFC. Curteanu et al. [36] developed an optimization multi-objective strategy and applied it to optimize a series of PEMFC parameters. Yang et al. [37] used a GA to optimize the channel-to-rib ratio and suggested that channel-to-rib widths of 2.8:0.5 and 4.2:0.3 are best fitted. Zeng et al. [38] optimized the width of the bottom and top edges of the PEMFC channel using a GA. Cai et al. [39] designed a bioinspired wavelike structure and applied it to a fuel cell channel. Subsequently, they performed the structure using a GA. By setting the ratio of the pressure drop loss to the output power as the objective function, Huang et al. [40] optimized the channel structure of a high-temperature PEMFC using the GA. Zhou et al. [41] divided the flow channel of a PEMFC into several segments and optimized the parameter design using a GA. Yu et al. [42] presented a novel 3D fine-mesh flow field of a PEMFC and used a GA and non-dominated sorting genetic algorithm to optimize the geometric parameters of the flow field.

Considering the aforementioned studies, research on the flow field of PEMEC has mainly focused on comparing the performances of different flow-field patterns or designing new flow fields. However, the structural parameters of the flow field still have significant potential for further study. For PEMFC, the GA can also be a competitive method used to optimize the geometric parameters of PEMEC. In this study, a 3D PEMEC channel model was developed using the COMSOL Multiphysics software. Using the model, the influence of channel height and width was assessed in preparation for subsequent optimization. Furthermore, through the link between MATLAB and COMSOL, a complete PEMEC model with a parallel flow-field pattern was created, and its channel heights and widths were optimized using GA to obtain an optimized flow-field pattern and lower energy consumption.

2. Model description

2.1. *Physical model*

Attaching materials each components used, the physical structure of the PEMEC channel model is shown in Fig. 1, including an anode/cathode bipolar plate (ABP/CBP), an anode/cathode channel (ACH/CCH), an anode/cathode porous transport layer (APTL/CPTL), an anode/cathode catalyst layer (ACL/CCL), and a proton exchange membrane (PEM). The geometric and operational parameters are listed in Tables 1 and 2, respectively. In addition, the thermodynamic parameters of the materials unlisted in Table 2 could obtained from the COMSOL material database.

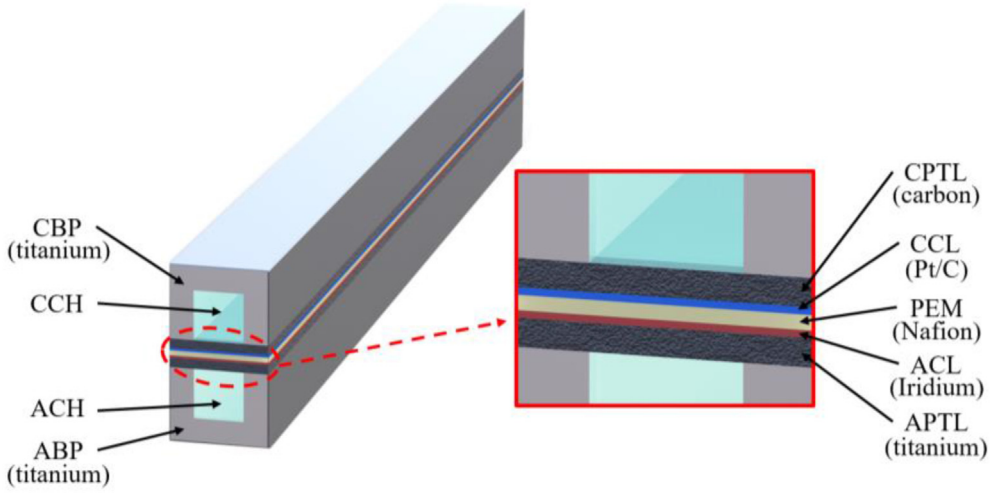

Fig. 1 – Channel model.

Table 1 – Geometrical parameters of the channel model [43].

Geometrical Parameters	Value
reaction area	100 mm^2 (50 mm × 2 mm)
BP height	1.5 mm
BP width	1.5 mm
PTL thickness	0.3 mm
CL thickness	0.02 mm
PEM thickness	0.178 mm

Table 2 – Operation parameters [24,44–47].

Parameters (symbol)	Value
Anode charge transfer coefficient (α_a)	0.5
Cathode charge transfer coefficient (α_c)	0.5
Anode reference exchange current density ($i_{0,a}$)	0.1 A/m^2
Cathode reference exchange current density ($i_{0,c}$)	10000 A/m^2
Electron conductivity (σ_s)	1000 S/m
Porosity of porous transport layer (ε_{PTL})	0.5
Porosity of catalyst layer (ε_{CL})	0.25
Permeability of porous transport layer (K_{PTL})	1×10^{-12} m^2
Permeability of catalyst layer (K_{CL})	1×10^{-13} m^2
Operating pressure (P_{op})	1 atm
Operating temperature (T_{op})	60 °C
Inlet volumetric flowrate (Q_{in})	15 mL/min

2.2. Governing equations

To simplify the model, we made the following assumptions: water was always in the liquid state, single-phase flow was used to calculate the velocity and pressure distribution of the fluid, hydrogen and oxygen produced were ideal incompressible gases, the gas cross-permeation effect was negligible, PTL and CL were isotropic, the flow pattern of the fluid within channels was laminar, and the water content in the membrane was always saturated.

Corresponding to the physical fields in COMSOL, the governing equations of the model were divided into three parts: electrochemistry, fluid mechanics, and thermodynamics.

2.2.1. Electrochemistry

Electrochemistry (PEMEC) module simulates the electrochemical reaction process and provides the distributions of potential, current density, and gas concentration for the results.

Electrochemical reactions at the cathode and anode within the PEMEC can be represented using the Butler–Volmer equation [48]: Eqs. (1) and (2), as follows:

$$i_{v,a} = a_{v,a}(1-\theta) i_{0,a}\left(\frac{C_{O_2}}{C_{0,O_2}}\right)\left[exp\left(\frac{\alpha_a F \eta_{act}}{RT}\right) - exp\left(\frac{-\alpha_c F \eta_{act}}{RT}\right)\right] \quad (1)$$

$$i_{v,c} = a_{v,c}(1-\theta) i_{0,c}\left(\frac{C_{H_2}}{C_{0,H_2}}\right)\left[exp\left(\frac{\alpha_a F \eta_{act}}{RT}\right) - exp\left(\frac{-\alpha_c F \eta_{act}}{RT}\right)\right] \quad (2)$$

where the active overpotential η_{act} reflects the energy barrier that must be overcome in the chemical reaction and was defined as [49].

$$\eta_{act} = \varphi_s - \varphi_e - V_{eq} = \varphi_s - \varphi_e - 1.229 + 9 \times 10^{-4}(T - 298.15) \quad (3)$$

Two potentials φ_s and φ_e are defined by charge conservation equations [50]:

$$\nabla \cdot (-\sigma_s \nabla \varphi_s) = S_{\varphi,s} \quad (4)$$

$$\nabla \cdot (-\sigma_m \nabla \varphi_e) = S_{\varphi,e} \quad (5)$$

The covering coefficient was introduced to represent the impact of the bubbles covering the electrodes on the current density, which could be defined as [51].

$$\theta = \left[-97.25 + 182\frac{T}{T^0} - 84\left(\frac{T}{T^0}\right)^2\right] * \left(\frac{j}{300000}\right)^{0.3} * \frac{1}{p - p_{sat}} \quad (6)$$

where p_{sat} is the saturated pressure of water.

Then, there was an ohmic overpotential in the PEMEC, representing the electrically conductive resistance of each component in the PEMEC:

$$\eta_{ohmic} = I\left(R_{bp} + R_{PTL} + R_{CL} + \frac{d_m}{A_m \sigma_m}\right) \quad (7)$$

In addition, conductivity was originally a function of the water content in the membrane and temperature. However, based on the assumptions, the water content in the membrane was assumed to be 14 [52]. Thus, the electrolyte conductivity could be expressed using Eq. (8) [53].

$$\sigma_m = 6.94\, exp\left[1268\left(\frac{1}{303} - \frac{1}{T}\right)\right] \quad (8)$$

Mass transport limitation in PEMEC led to concentration overpotential (or diffusion overpotential) [54].

$$\eta_{diff,a} = \frac{R_u T_a}{4F} ln \frac{C_{O_2,m}}{C^0_{O_2,m}} \quad (9)$$

$$\eta_{diff,c} = \frac{R_u T_c}{2F} ln \frac{C_{H_2,m}}{C^0_{H_2,m}} \quad (10)$$

The cell voltage could then be expressed using Eq. (11) [54]:

$$V = V_{eq} + \eta_{act} + \eta_{ohmic} + \eta_{diff,a} + \eta_{diff,c} \quad (11)$$

In contrast, the gas concentration in PEMEC was controlled by the species transport equation [24].

$$\nabla \cdot (\varepsilon_x \boldsymbol{u}_i C_i) = \nabla \cdot \left(D_{ij}^{eff} \nabla C_i\right) + S_i \quad (12)$$

where D_{ij}^{eff} represents the effective diffusion coefficient of specie "i" and specie "j". According to Bruggeman's equation, D_{ij}^{eff} could be expressed as Eq. (13) [55]:

$$D_{ij}^{eff} = \varepsilon_x^{1.5} D_{ij}^0 \left(\frac{T}{T_0}\right)\left(\frac{p_0}{p}\right) \quad (13)$$

2.2.2. Fluid mechanics

In this module, the velocity and pressure of the fluid are calculated.

The fluid velocity and pressure distributions were controlled by the continuity equation [56] and momentum conservation equation [24], respectively.

$$\nabla \cdot (\varepsilon_x \rho_{fm} \boldsymbol{u}_{fm}) = S_m \quad (14)$$

$$\nabla \cdot (\varepsilon_x \rho_{fm} \boldsymbol{u}_{fm} \boldsymbol{u}_{fm}) = -\varepsilon_x \nabla p + \nabla \cdot \left(\varepsilon_x \mu_{fm} \nabla \boldsymbol{u}_{fm}\right) + S_v \quad (15)$$

Table 3 – Source terms in governing equations [45].

Component	Expression
BP	$S_T = \frac{i_v^2}{\sigma_{BP}}$
PTL	$S_T = \frac{i_v^2}{\sigma_{PTL}}\ S_v = -\frac{\mu_{fm}}{K_{PTL}}\varepsilon_{PTL}^2 u_{fm}$
PEM	$S_T = \frac{i_v^2}{\sigma_m}$
ACL	$S_{\varphi,s} = i_v\ S_{\varphi,e} = -i_v\ S_v = -\frac{\mu_{fm}}{K_{CL}}\varepsilon_{CL}^2 u_{fm}$
	$S_{m,H_2O} = S_{H_2O} = \left(-\frac{i_v M_{H_2O}}{2F}\right)$
	$S_{m,O_2} = S_{O_2} = \frac{i_v M_{O_2}}{4F}\ S_T = i_v\eta_{a,act} + \frac{i_v^2}{\sigma_s} + \frac{i_v^2}{\sigma_m} - T\frac{dV_{eq}}{dT}$
CCL	$S_{\varphi,s} = -i_v\ S_{\varphi,e} = i_v\ S_v = -\frac{\mu_{fm}}{K_{CL}}\varepsilon_{CL}^2 u_{fm}\ S_{H_2} = S_m = \left(\frac{i_v M_{H_2}}{2F}\right)\ S_T = i_v\eta_{c,act} + \frac{i_v^2}{\sigma_s} + \frac{i_v^2}{\sigma_m}$

Even though the flow in the PEMEC was considered a single-phase flow, the impact of the hydrogen and oxygen volume fractions on the physical parameters of the flow could not be ignored. Therefore, the density and viscosity of the flow in Eqs. (14) and (15) were affected by liquid and gas, as shown in Eqs. (16) and (17) as follows:

$$\rho_{fm} = \rho_l\left(1-\phi_g\right) + \rho_g\phi_g \tag{16}$$

$$\mu_{fm} = \mu_l\left(1-\phi_g\right) + \mu_g\phi_g \tag{17}$$

2.2.3. *Thermodynamics*

Thermodynamics calculates the temperature distribution of PEMEC using the energy conservation equation [48].

$$\nabla\cdot\left(\rho^{eff}C_p^{eff}\mathbf{u}_i\right)T = \nabla\cdot\left(k^{eff}\nabla T\right) + S_T \tag{18}$$

The PTL and CL in the PEMEC are porous media, and their effective density, specific heat capacity, and thermal conductivity were defined by Eq. (19)–(21) [45]:

$$\rho^{eff} = (1-\varepsilon_x)\rho_{sa} + \varepsilon_x\rho_{fm} \tag{19}$$

$$C_p^{eff} = (1-\varepsilon_x)C_{p,sa} + \varepsilon_x C_{p,fm} \tag{20}$$

$$k^{eff} = (1-\varepsilon_x)k_{sa} + \varepsilon_x k_{fm} \tag{21}$$

Source terms in governing equations are shown in Table 3.

2.3. *Boundary condition*

The selected boundaries and corresponding boundary conditions are illustrated in Fig. 2. The adiabatic boundary surfaces 1 and 2 were set to electrical grounding and constant current density, respectively. Water flows in the PEMEC from boundary surfaces 3 and 4 at a constant temperature and flow rate, and exits through boundary surfaces 5 and 6 at a constant pressure. Not mentioned boundaries include insulation and adiabatic solid walls.

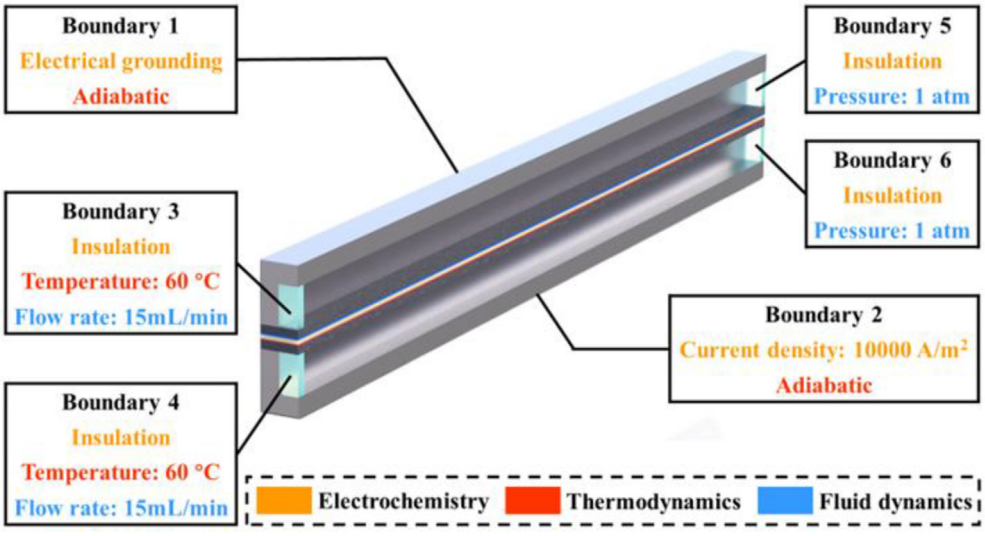

Fig. 2 – Boundary modifying and corresponding boundary conditions.

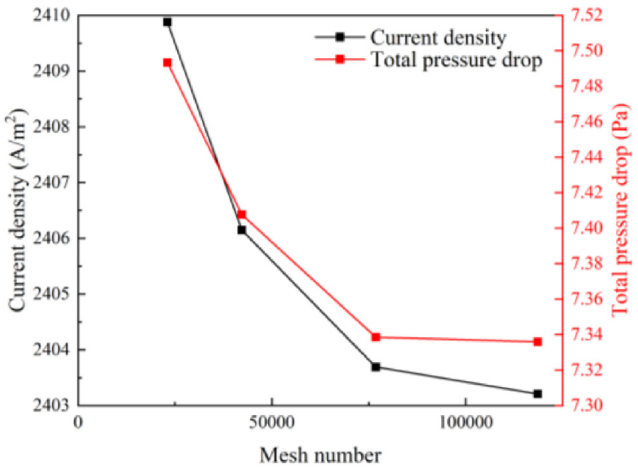

Fig. 3 – Test of mesh independence.

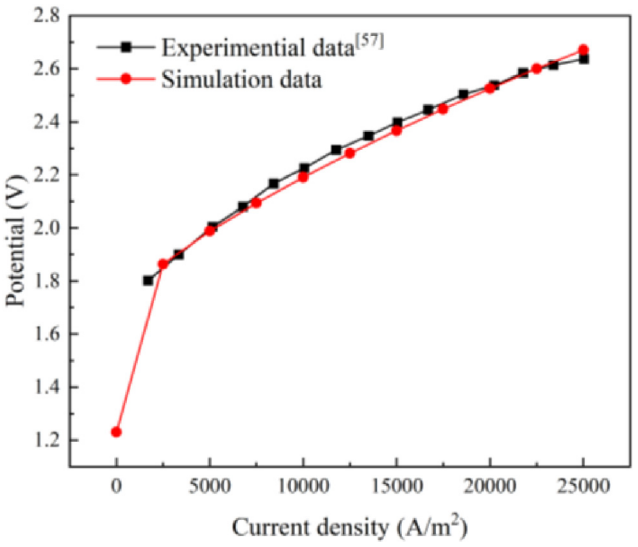

Fig. 4 – Comparison of polarization curves between simulation and experiment.

2.4. *Numerical implementation*

The commercial software COMSOL Multiphysics was used to calculate the governing equations using the finite element method. To test mesh independence, four different numbers of structured grids were adopted, including 23040, 42400, 76800, and 118560 elements. The test results are shown in Fig. 3. For an operating voltage of 1.8 V, the relative errors of the current density and the sum of the pressure drops in the anode and cathode of the grid systems with 76800 and 118560 elements were approximately 0.02% and 0.35%, respectively, indicating that the 76800 elements model meets the requirements for calculation accuracy.

2.5. *Model validation*

To ensure the accuracy of the channel model, its polarization curve was compared with the experimental data from Majasan et al. [57]. The results are illustrated in Fig. 4, where the average deviation rate between the two curves was 0.92%. Therefore, the model was considered sufficiently reliable for reflecting the experimental results.

3. Results and discussion

3.1. *Relationship between channel height and PEMEC performance*

To explore the impact of channel height changes on the voltage, pressure drop, and the ability to discharge gas, channel width was fixed to 1 mm and channel height was changed using a series of values (from 0.3 mm to 1.5 mm) in the operating condition where the current density was 10000 A/m^2, the volumetric flowrate was 15 mL/min, and the operation temperature, i.e. the temperature of water at the entrance of the cathode and anode channels, was 60 °C.

As shown in Fig. 5, decreasing the channel height might increase the flow velocity within the channel. Furthermore, a

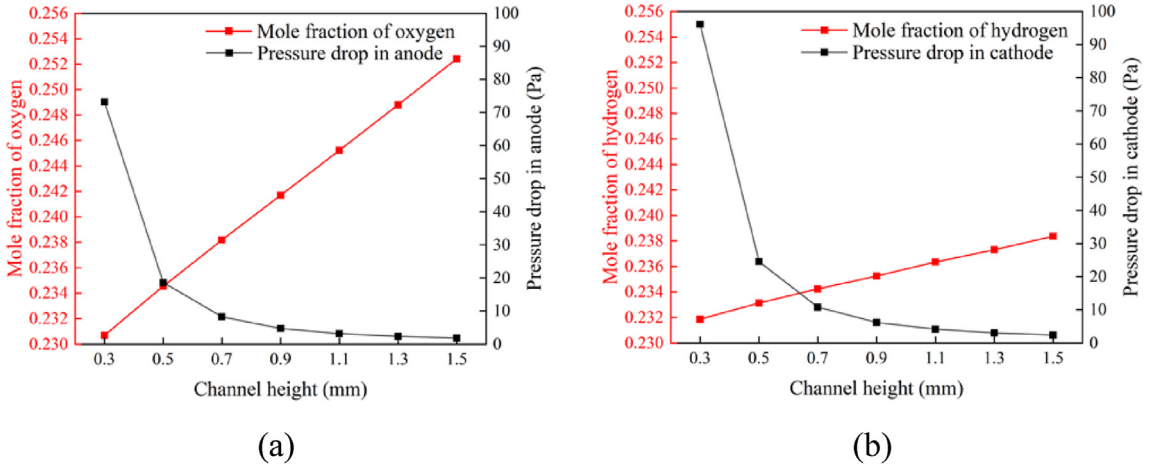

Fig. 5 – Effect of channel height on the gas mole fraction and pressure drop: (a) anode, (b) cathode.

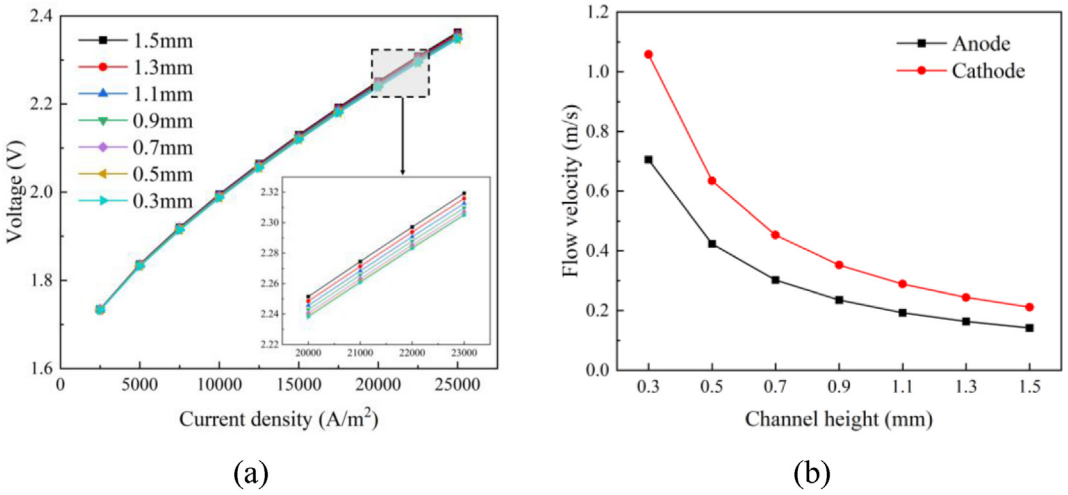

Fig. 6 – Polarization curves and velocity in channel at different channel heights: (a) polarization curves, (b) velocity.

higher flow velocity could promote gas discharge within the anode and cathode channels, which was conducive to the efficient and stable operation of PEMEC. However, the pressure drop increased with decreasing channel height, particularly when the channel height was small.

For the next phase of optimization, the lower limit for the channel height was set to 0.5 mm to prevent an excessive pressure drop and improve the efficiency of the algorithm.

The polarization curves and flow velocities at different channel heights are shown in Fig. 6. An increase in channel height led to a gradual increase in voltage. Nafchi et al. [26] observed similar results. These phenomena can be interpreted as changes in channel height, which mainly affect the cell voltage by changing the concentration overpotential. As described above, a higher channel height might lead to a lower flow velocity and decreased gas discharge ability. Hence, the gases accumulated in the APTL/CPTL increase the mass-transfer resistance, which meant that the PEMEC has a higher concentration overpotential.

3.2. *Relationship between channel width and PEMEC performance*

Under the same operating conditions, the impact of channel width changes was investigated on the premise of a 1 mm channel height. Under constant flow rate conditions, a narrower channel width corresponded to a higher flow velocity, as shown in Fig. 7. However, in this case, the mole fractions of oxygen and hydrogen within the anode and cathode exhibited the same trend as the flow velocity, which was completely opposite to the effects of channel height change. A graphical representation of this phenomenon is shown in Fig. 8. Under the channel and ribs, the difference in the hydrogen mole fraction within the CPTL was evident, and the boundaries of the mole fraction mutation were closely related to the boundaries between the channel and ribs. This was explained by the fact that gases under ribs have a longer distance to diffuse into the channel and the negative influence of a longer diffusion distance is greater than the positive influence of the increased flow velocity, leading to an impaired ability to discharge gas.

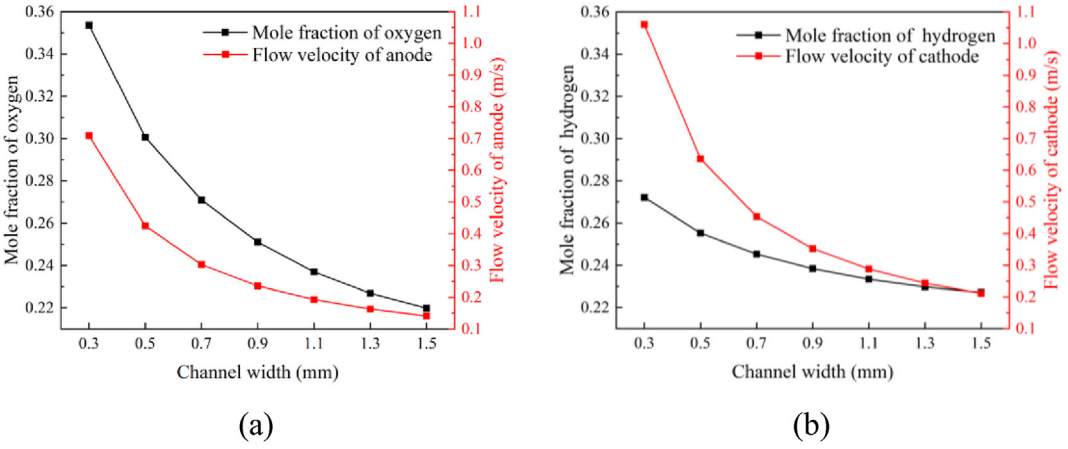

Fig. 7 – Effect of channel width on the gas mole fraction and flow velocity: (a) anode, (b) cathode.

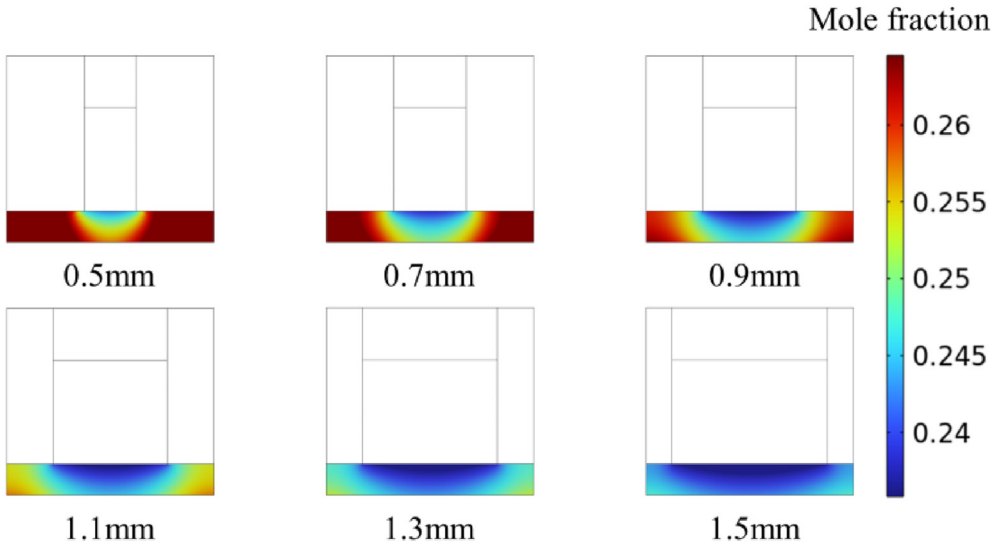

Fig. 8 – Hydrogen mole fraction in cross section of CPTL.

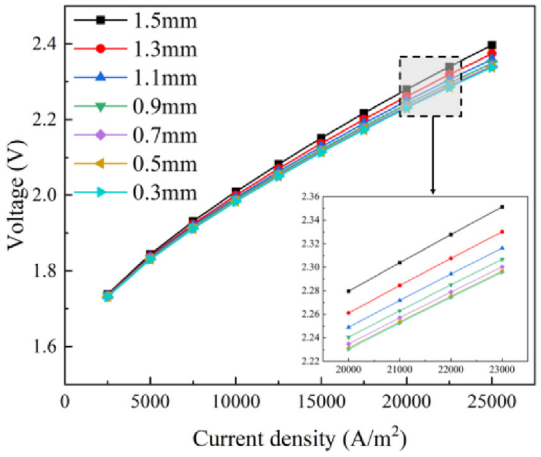

Fig. 9 – Polarization curves at different channel widths.

Based on the relationship between the channel width and the PEMEC performance, the lower limit for the width in the next stage of optimization was set to 0.7 mm to avoid gas discharging deterioration.

Although the gas mole fractions and the concentration overpotential decrease with an increase in channel width, the voltage had a clear increase associated with this change, and the increasing rates were more obvious than those associated with changes in channel height (Fig. 9), in accordance with the research by Zhang et al. [28]. The increase in the channel width reduced the contact area between the BP and PTL, which in turn led to an increase in the transfer resistance of electrons (i.e., the ohmic overpotential). Subsequently, the increase in the ohmic overpotential offsets the decrease in the concentration overpotential, enhancing the cell voltage.

3.3. *Optimization of PEMEC with parallel flow field pattern*

In this section, we established a complete PEMEC model and optimized its height and width using a GA to improve its performance. MATLAB was chosen as the platform for the GA operation, and COMSOL was used to model the computations and provide the fitness degree to the GA. The software was integrated using the COMSOL software interface. Fig. 10 illustrates the optimization process in detail. The loop between COMSOL and MATLAB can generate new variables, update the numerical simulation, and search for optimization automatically. The initial population, which included several PEMEC models with different structural parameters, was created using the GA in MATLAB and sent to COMSOL through the software interface to calculate the fitness. Subsequently, the fitness was returned to MTALAB as the criterion for screening superior individuals in the population. The selected individuals generated the next population after a series of operations, including heredity, crossover, and variation, and the new population was sent to COMSOL to begin the next circle.

3.3.1. *Model establishing and validation*

Fig. 11 illustrates the structure of the model, and Table 4 lists its geometrical parameters. We chose a parallel flow field as the optimization object because it was one of the most common flow-field patterns in electrolysis cells. The complete model has identical thicknesses of the PTL, CL, and PEM as the single-channel model, and we controlled both to have close reaction areas. Fig. 12 illustrates the mesh independence test results and a comparison of the polarization curves to demonstrate the reliability of the model. The relative errors of the current density and pressure drop between grid systems with 251563 and 504497 elements were approximately 0.18% and 0.006%, respectively; therefore, we considered 251563 as the appropriate mesh number. Similar to the channel model, the average deviation rate between the two curves was approximately 0.90%.

3.3.2. *Configuring of optimization*

There were two main sources of energy consumption for PEMEC. One was the power consumption by electrolytic reactions, and the other was associated with a pump that

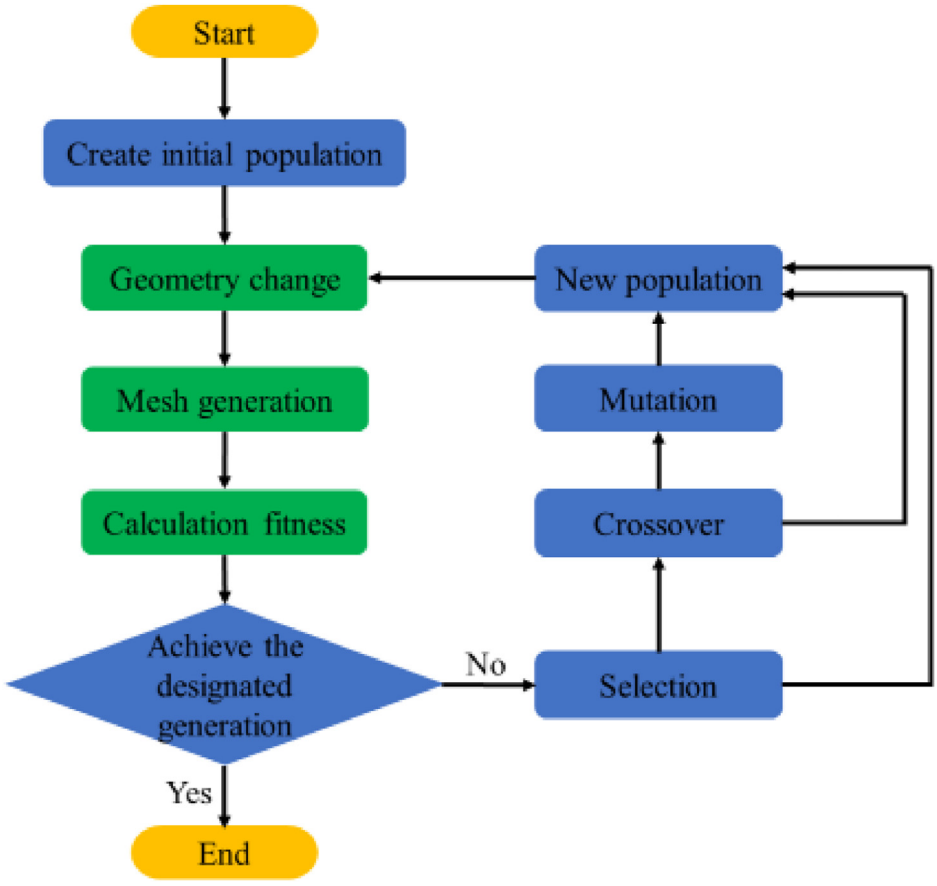

Fig. 10 – Flow chart of the optimization process.

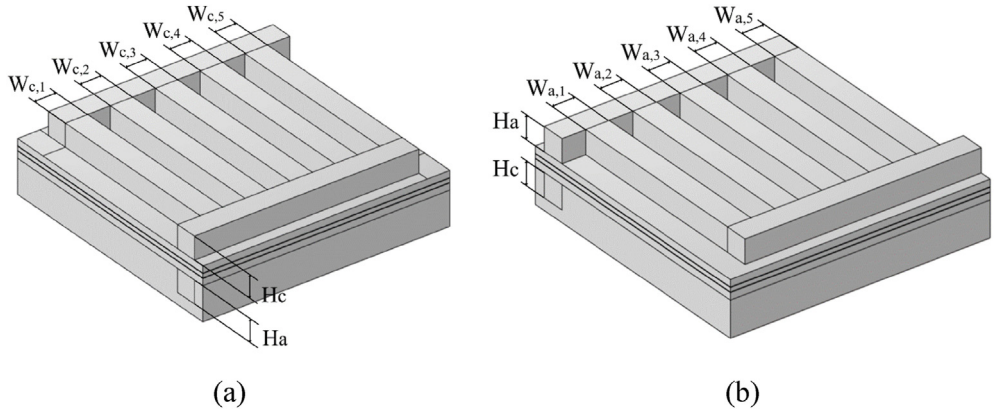

Fig. 11 – Complete PEMEC model with parallel flow field pattern: (a) cathode, (b) anode.

Table 4 – Geometrical parameters of the complete model [43].

Geometrical Parameters	Value
reaction area	121 mm^2 (11 mm × 11 mm)
inlet channel length	10 mm
outlet channel length	10 mm
parallel channel length	8 mm
PTL thickness	0.3 mm
CL thickness	0.02 mm
PEM thickness	0.178 mm

pumps water into the anode and cathode. These were defined as follows:

$$P_r = V_{cell} I \tag{22}$$

$$P_p = \Delta p_a Q_a + \Delta p_c Q_c = Q_{in}(\Delta p_a + \Delta p_c) \tag{23}$$

In Eqs. (22) and (23), V_{cell} is the operational voltage of the PEMEC, and I is the operational current, i.e., the product of the current density and activated area. Δp and Q represent the pressure drop and flow rate, respectively. Because of the constants I and Q_{in} in this case, P_r and P_p are determined by

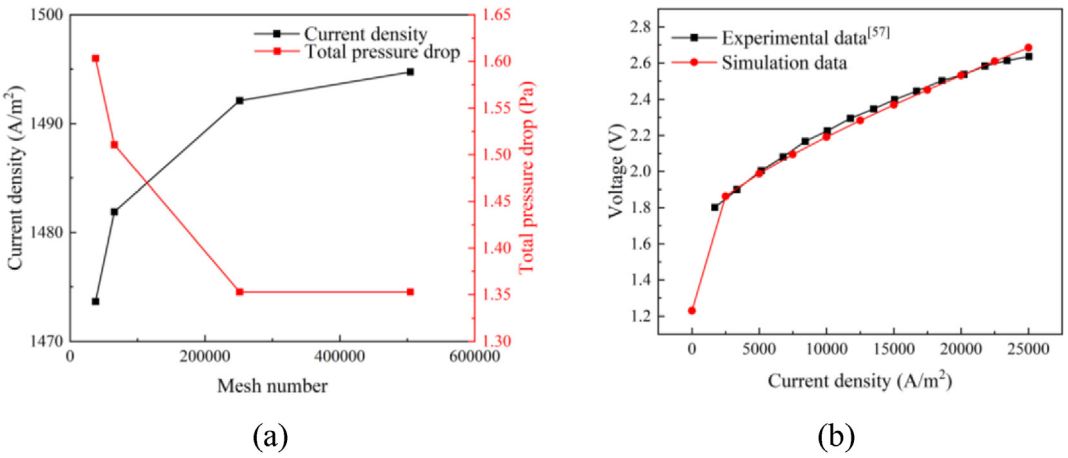

Fig. 12 – Model validation of the complete model: (a) test of mesh independence, (b) comparison of polarization curves between experiment and simulation.

V_{cell}, Δp_a, and Δp_c. To improve the feasibility of the solution, Δp was defined as the sum of Δp_a and Δp_c. Therefore, the purpose of the GA was expressed as:

$$\min\left[P_r, P_p\right] = \min\left[V_{cell}, \Delta p\right] \quad (24)$$

As described in sections 3.1 and 3.2, if the PEMEC achieves a low voltage, the pressure drop in the anode and cathode will be high, and vice versa. Hence, there was a tradeoff between V_{cell} and Δp.

Furthermore, the widths of the five channels of the PEMEC and the heights of the anode and cathode were considered as variables. The following constraints were imposed on the variables:

$$0.7\ m\ m \le W_{a,i} = W_{c,i} \le 1.9\ m\ m\ (i = 1, 2, 3, 4, 5)$$

$$0.5\ m\ m \le H_a, H_c \le 1.4\ m\ m$$

The lower limits of all variables are given in sections 3.1 and 3.2 and their upper limits are constrained by the geometry of the model. To prevent low-quality meshes, channels with the same serial numbers for the anode and cathode had equal widths (i.e., $W_{a,i} = W_{c,i}$). In this study, to maintain calculation accuracy, we used seven variables, two optimization objectives, a population of 40, and a generation number of 40 for the GA. In addition, the operating current density and pressure were respectively set at 10000 A/m^2 and 1 atm, with a flow rate of 15 mL/min and temperature of 60 °C (333.15 K).

3.4. *Optimization results*

Table 5 lists the geometrical parameters of the original and optimized models. The channel widths decreased to different degrees, and the heights of the anode and cathode increased. The reason for this phenomenon happened can be found in Figs. 6 and 9. Owing to the respective characteristics of the concentration overvoltage and ohmic overvoltage, the effect of the channel width on the cell voltage was more remarkable than that of the channel height; thus, the GA tended to reduce the voltage by reducing the width of the channels while increasing the channel heights to control the pressure drops in the anode and cathode.

Table 5 – Geometrical parameters of original and optimized models.

	Original model	Optimized model
W_1	1 mm	0.8465 mm
W_2	1 mm	0.7388 mm
W_3	1 mm	0.8904 mm
W_4	1 mm	0.8315 mm
W_5	1 mm	0.7938 mm
H_a	1 mm	1.2477 mm
H_c	1 mm	1.3979 mm

As shown in Fig. 13, the optimized model has a lower voltage than the original model because the width of all the channels decreases, which means that the optimized model can run more efficiently. Meanwhile, the voltage change rate increased as the current density increased, and the maximum value in the figure appeared at the 35000 A/m^2 current density of 0.26%. In addition, as BPs are made of titanium, an element with relatively high electrical conductivity, changing the widths to reduce the ohmic resistance only has a limited role,

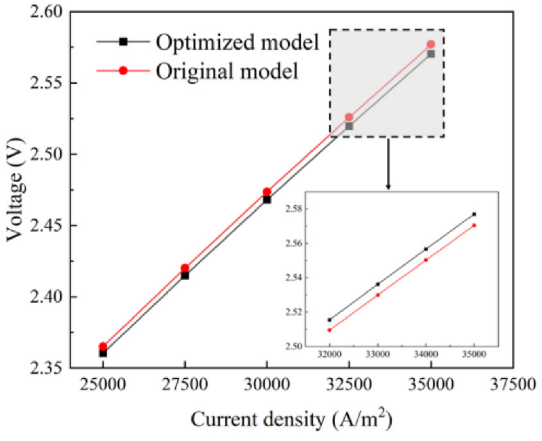

Fig. 13 – Partial polarization curves of the optimized and original models.

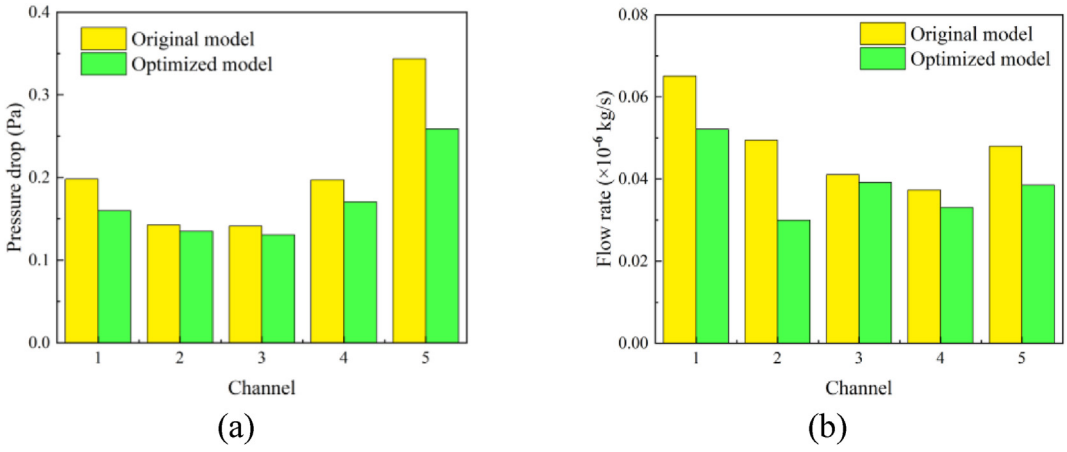

Fig. 14 – Pressure drop and flow rate in each cathode channel of the original and optimized models: (a) pressure drop distribution (standard deviations of original and optimized models are 0.08 and 0.05, respectively); (b) flow rate distribution (standard deviations of original and optimized models are 0.01 and 0.008, respectively).

and the voltage difference between the original and optimized models is not obvious, especially for low current densities.

Under the premise of narrowing channels, one method to obtain a lower pressure drop is to increase the channel heights, whereas the other is to adjust the channel widths to make them more consistent with the flow characteristics and reduce the flow resistance. Fig. 14 illustrates the pressure drop and flow rate in each channel of the optimized and original models. Compared with the original model, the pressure drops of each channel in the optimized model are decreased at different degrees while Δp decreases by 34.97% (from 1.82 Pa to 1.18 Pa). The flow rate in each channel also decreases. In contrast to Table 5 and Fig. 14, it is worth noting that a channel with lower pressure drop and flow rate had a lighter width reduction (e.g., channels 3 and 4). As a result, the decreasing range of the pressure drop or flow rate within it is relatively small, and the optimized model was characterized by more uniform pressure drop and flow rate distributions, which means that the optimized flow field pattern was more appropriate for PEMEC. The optimization result can be observed in Fig. 15 more intuitively.

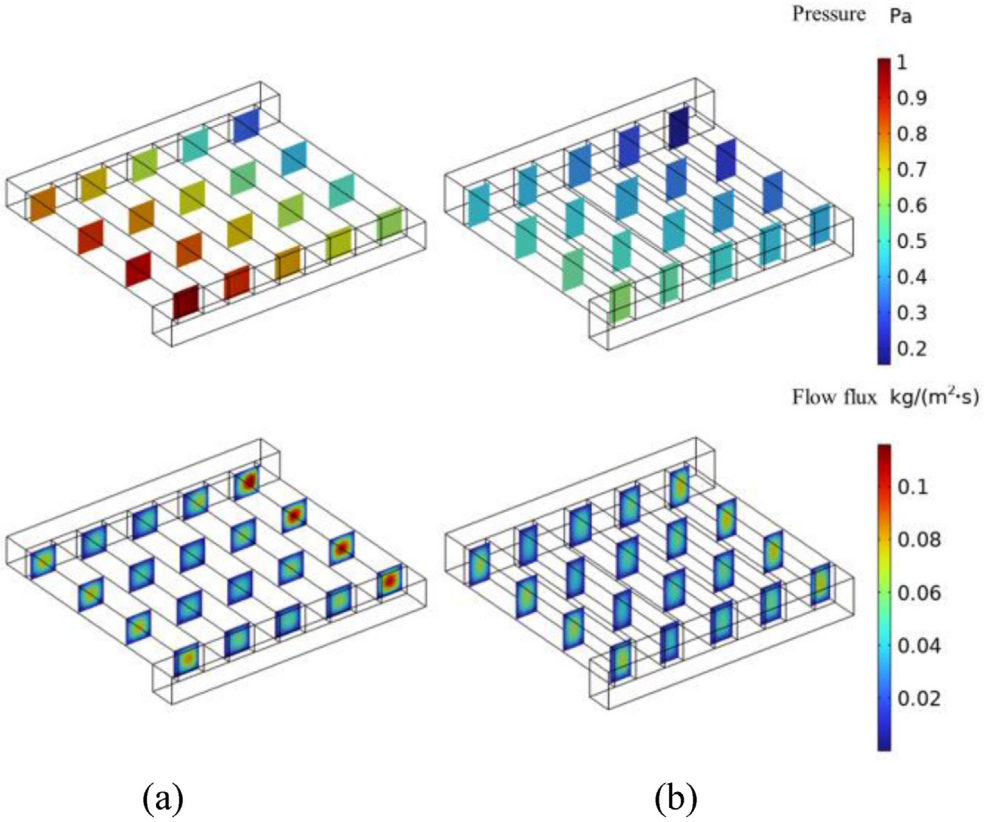

Fig. 15 – Pressure and flow flux in sections of the cathode channel: (a) original model, (b) optimized model.

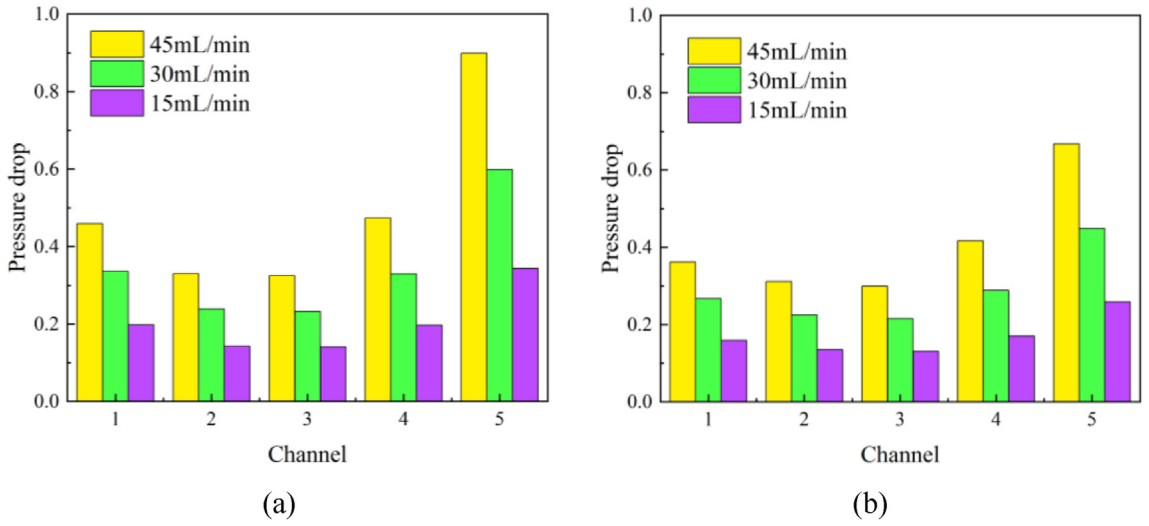

Fig. 16 – Pressure drop of each cathode channels at different flow rates: (a) original model, (b) optimized model.

Through optimization, both the pressure difference between the inlet and outlet of each channel (i.e., the pressure drop in the channel) and the pressure difference between channels were reduced. Furthermore, the final channel with the highest flow flux among the original model was almost the same as the other channels in the optimized model.

Moreover, the optimization impact became more evident as the flow rate increased (Fig. 16). For different flow rates, the optimized model exhibited an improved pressure drop compared with that of the original model. In addition, for the optimization model, the pressure drop exhibited a lighter overshoot when the flow rate changed, particularly for the final channel. However, it could not be ignored that the final channel always exhibited the highest value and increased rate of pressure drop among all channels in every situation. Thus, in future studies, the constraints of the height and width of the final channel could be considered separately from those of the other channels, considering computational efficiency and optimization results.

As a benefit of the optimized flow-field pattern, the current density distribution in the proton exchange membrane improved and became more uniform owing to a more uniform flow rate (Fig. 17). The edge and corner areas of the membrane exhibit lower current densities in the optimized model. Similar changes were observed below the ribs. Alternatively, the area with undersized current density under the channels was reduced. These changes indicated that each point on the CLs of the optimized model had a more similar reaction speed. Thus, compared with the original model, the high gas holdup for a partial position in the PTLs could be ameliorated, especially at the corners and locations under the ribs, which could not be covered by channels and have a lower ability to discharge gas.

As shown in Fig. 18 (a) and (b), as a result of using narrower and taller channels, the hydrogen mole fractions within the

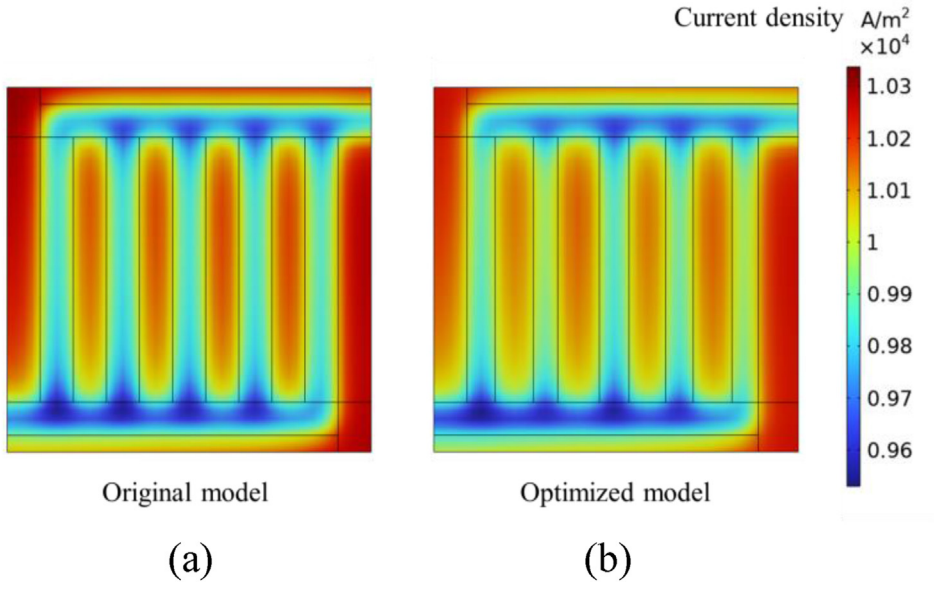

Fig. 17 – Current density distribution in proton exchange membranes: (a) original model, (b) optimized model.

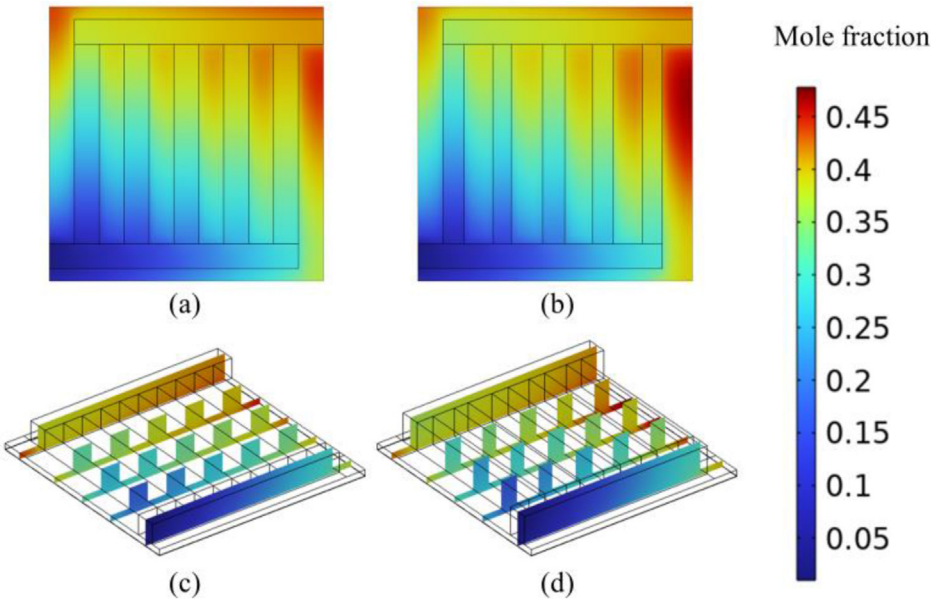

Fig. 18 – Hydrogen fraction in the cathode: (a) vertical view of original model, (b) vertical view of optimized model, (c) sectional view of original model, (d) sectional view of optimized model.

channels and CPTL were increased, especially in the part proximal to the channel exits. However, owing to the constraint on the lower width limit and the optimized flow-field pattern, the magnitude of the increase in the hydrogen mole fraction is acceptable. In addition, it was noteworthy that in the upper left corner of the optimized model, unlike other positions, the hydrogen fraction exhibited a small decline, which might be explained by the uniform current density distribution. A similar conclusion could be drawn from the sectional views as Fig. 18 (c) and (d).

Fig. 19 shows the molar fraction of oxygen in the anode. Unlike the situation in the cathode, the oxygen mole fraction was significantly higher than that of the hydrogen in the cathode, and no region in the anode had a lower mole fraction following optimization, even though the number of moles of hydrogen produced per second was theoretically twice that of oxygen. This indicated that changes in the channel height and width have a marked effect on the oxygen mole fraction but not on the hydrogen mole fraction. This conclusion was corroborated by a comparison of Fig. 5 as well as Fig. 7. The

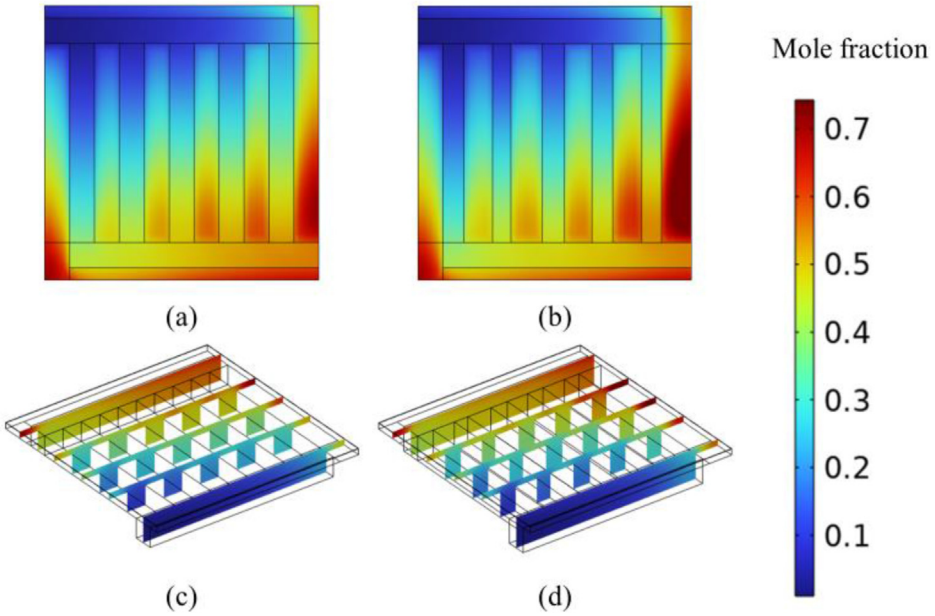

Fig. 19 – Oxygen fraction in anode: (a) vertical view of original model, (b) vertical view of optimized model, (c) sectional view of original model, (d) sectional view of optimized model.

basic cause of this difference was that the diffusivity of hydrogen was approximately 3.4 times that of oxygen, making hydrogen more easily discharged from channels of different sizes than oxygen. Therefore, in future studies, to ensure the ability of the gas to be discharged within the anode, it would be necessary to consider different optimization configurations for the anode and cathode.

Then, the efficiency of PEMEC can be defined as [58]:

$$\eta_{en} = \frac{N_{out} * LHV_{H_2}}{P_r + P_p} = \frac{N_{out} * LHV_{H_2}}{IV + Qp} \tag{25}$$

Because of the constant flow rate and temperature of the feed water, the hydrogen production and water consumption rates of the original and optimized models were very close. However, the optimized channel structure restricts the ability to discharge gas, leading to a lower hydrogen mass flow rate at the cathode outlet (N_{out}) in the optimized model. Although the cell voltage and pressure drop decreased after optimization, the efficiency of the optimized system decreased at low amplitudes (from 65.50% to 64.26%). Thus, the impact of the channel structure on PEMEC performance has further research value.

4. Conclusion

In this study, a 3D non-isothermal PEMEC channel model was developed using COMSOL Multiphysics to study the impact of channel height and width on the performance of PEMEC. By linking COMSOL Multiphysics with MATLAB, a complete PEMEC model with a parallel flow-field pattern was obtained and optimized via a GA. The optimized model was then compared with the original model. Based on our simulation results, we reached the following conclusions.

1. Increasing the channel height can lead to a simultaneous increase in the gas fraction and voltage within the PEMEC but a decrease in the pressure drop. Conversely, increasing the channel width can lead to a higher voltage and lower pressure drop, while the gas fraction increases. In addition, the effect of channel width on voltage was more significant than that of channel height.
2. Through optimization, the optimized model decreased the pressure drop by 34.97% at a lower voltage. Because the effect of the channel width on the voltage was more significant than that of the channel height, the GA preferred to reduce the voltage by reducing the width of the channels, whereas the channel heights were increased to control the pressure drop within the anode and cathode.
3. By making the flow-field pattern more consistent with the flow characteristics, the pressure drop and flow rate in each channel become more uniform. Furthermore, the optimized flow field pattern led to a more homogeneous current density distribution on the proton exchange membrane and reduced the gas holdup for a partial position in the cathode; however, the gas fraction in the whole anode was increased. Hence, it is necessary to consider different optimization configurations for the anode and cathode.
4. Owing to its poor gas discharge ability, the hydrogen mass flow rate in the optimized cathode outlet decreased, leading to a lower efficiency after optimization, even though the power consumption of the PEMEC improved. The impact of the channel structure on PEMEC performance has further research value.

Declaration of competing interest

The authors declare that they have no known competing financial interests or personal relationships that could have appeared to influence the work reported in this paper.

Acknowledgments

This work was supported by the National Key Research and Development Program of China (No. 2022YFB4003801), the National Natural Science Foundation of China (Grant No. 52076088), and the Core Technology Research Project of Shunde District, Foshan City, China (No.2130218002932).

REFERENCES

[1] Bilgen S. Structure and environmental impact of global energy consumption[J]. Renew Sustain Energy Rev 2014;38:890–902.
[2] Salari A, Hakkaki-Fard A. A numerical study of dust deposition effects on photovoltaic modules and photovoltaic-thermal systems. Renew Energy 2019;135:437–49.
[3] Yang Y, Bremner S, Menictas C, et al. Battery energy storage system size determination in renewable energy systems: a review. Renew Sustain Energy Rev 2018;91:109–25.
[4] Zhang F, Zhao P, Niu M, et al. The survey of key technologies in hydrogen energy storage. Int J Hydrogen Energy 2016;41(33):14535–52.
[5] Chi J, Yu H. Water electrolysis based on renewable energy for hydrogen production. Chin J Catal 2018;39(3):390–4.
[6] Nguyen T, Abdin Z, Holm T, et al. Grid-connected hydrogen production via large-scale water electrolysis. Energy Con Manage 2019;vol. 200:112108.
[7] Gerloff N. Comparative Life-Cycle-Assessment analysis of three major water electrolysis technologies while applying various energy scenarios for a greener hydrogen production. J Energy Storage 2021;43:102759.
[8] Carmo M, Fritz DL, Mergel J, et al. A comprehensive review on PEM water electrolysis. Int J Hydrogen Energy 2013;38(12):4901–34.
[9] Liu X, Liu G, Xue J, et al. Hydrogen as a carrier of renewable energies toward carbon neutrality: state-of-the-art and challenging issues. Int J Miner Metall Mater 2022;29(5):1073–89.
[10] Medina P, Santarelli M. Analysis of water transport in a high pressure PEM electrolyzer. Int J Hydrogen Energy 2010;35(11):5173–86.
[11] Zhang H, Su S, Lin G, et al. Efficiency calculation and configuration design of a PEM electrolyzer system for hydrogen production. Int J Electrochem Sci 2012;7(4):4143–57.
[12] Chandesris M, Médeau V, Guillet N, et al. Membrane degradation in PEM water electrolyzer: numerical modeling and experimental evidence of the influence of temperature

and current density[J]. Int J Hydrogen Energy 2015;40(3):1353–66.
[13] Ojong ET, Kwan JTH, Nouri-Khorasani A, et al. Development of an experimentally validated semi-empirical fully-coupled performance model of a PEM electrolysis cell with a 3-D structured porous transport layer. Int J Hydrogen Energy 2017;42(41):25831–47.
[14] Liso V, Savoia G, Araya SS, et al. Modelling and experimental analysis of a polymer electrolyte membrane water electrolysis cell at different operating temperatures. Energies 2018;11(12):3273.
[15] Toghyani S, Fakhradini S, Afshari E, et al. Optimization of operating parameters of a polymer exchange membrane electrolyzer. Int J Hydrogen Energy 2019;44(13):6403–14.
[16] Correa G, Marocco P, Muñoz P, et al. Pressurized PEM water electrolysis: dynamic modelling focusing on the cathode side. Int J Hydrogen Energy 2022;47(7):4315–27.
[17] Upadhyay M, Kim A, Paramanantham SSS, et al. Three-dimensional CFD simulation of proton exchange membrane water electrolyser: performance assessment under different condition[J]. Appl Energy 2022;306:118016.
[18] Qian X, Kim K, Jung S. Multiphase, multidimensional modeling of proton exchange membrane water electrolyzer. Energy Convers Manag 2022;268:116070.
[19] Zhao D, He Q, Wu X, et al. Modeling and optimization of high temperature proton exchange membrane electrolyzer cells. Int J Green Energy 2022;19(9):919–30.
[20] Salari A, Hakkaki-Fard A, Jalalidil A. Hydrogen production performance of a photovoltaic thermal system coupled with a proton exchange membrane electrolysis cell[J]. Int J Hydrogen Energy 2022;47(7):4472–88.
[21] Zhang X, Wang B, Xu Y, et al. Effects of different loading strategies on the dynamic response and multi-physics fields distribution of PEMEC stack. Fuel 2023;332:126090.
[22] Ruiz DDH, Sasmito AP, Shamim T. Numerical investigation of the high temperature PEM electrolyzer: effect of flow channel configurations. ECS Trans 2013;58(2):99.
[23] Tijani AS, Barr D, Rahim AHA. Computational modelling of the flow field of an electrolyzer system using CFD. Energy Proc 2015;79:195–203.
[24] Toghyani S, Afshari E, Baniasadi E, et al. Thermal and electrochemical analysis of different flow field patterns in a PEM electrolyzer. Electrochim Acta 2018;267:234–45.
[25] Toghyani S, Afshari E, Baniasadi E. Metal foams as flow distributors in comparison with serpentine and parallel flow fields in proton exchange membrane electrolyzer cells. Electrochim Acta 2018;290:506–19.
[26] Nafchi FM, Afshari E, Baniasadi E, et al. A parametric study of polymer membrane electrolyser performance, energy and exergy analyses. Int J Hydrogen Energy 2019;44(34):18662–70.
[27] Olesen AC, Frensch SH, Kær SK. Towards uniformly distributed heat, mass and charge: a flow field design study for high pressure and high current density operation of PEM electrolysis cells. Electrochim Acta 2019;293:476–95.
[28] Zhang Z, Xing X. Simulation and experiment of heat and mass transfer in a proton exchange membrane electrolysis cell. Int J Hydrogen Energy 2020;45(39):20184–93.
[29] Jia Y, Zeng M, Barnoon P, et al. CFD simulation of time-dependent oxygen production in a manifold electrolyzer using a two-phase model. Int Commun Heat Mass Tran 2021;126:105446.
[30] Chen Z, Wang X, Liu C, et al. Numerical investigation of PEM electrolysis cell with the new interdigitated-jet hole flow field. Int J Hydrogen Energy 2022;47(78):33177–94.
[31] Wu L, Zhang G, Xie B, et al. Integration of the detailed channel two-phase flow into three-dimensional multi-phase simulation of proton exchange membrane electrolyzer cell[J]. Int J Green Energy 2021;18(6):541–55.
[32] Wu L, An L, Jiao D, et al. Enhanced oxygen discharge with structured mesh channel in proton exchange membrane electrolysis cell. Appl Energy 2022;323:119651.
[33] Mert SO, Özçelik Z, Özçelik Y, et al. Multi-objective optimization of a vehicular PEM fuel cell system. Appl Therm Eng 2011;31(13):2171–6.
[34] Ohenoja M, Leiviskä K. Validation of genetic algorithm results in a fuel cell model. Int J Hydrogen Energy 2010;35(22):12618–25.
[35] Cheng SJ, Miao JM, Wu SJ. Use of metamodeling optimal approach promotes the performance of proton exchange membrane fuel cell (PEMFC). Appl Energy 2013;105:161–9.
[36] Curteanu S, Piuleac CG, Linares JJ, et al. Neuro-evolutionary approach applied for optimizing the PEMFC performance. Int J Hydrogen Energy 2014;39(8):4037–43.
[37] Yang WJ, Wang HY, Lee DH, et al. Channel geometry optimization of a polymer electrolyte membrane fuel cell using genetic algorithm. Appl Energy 2015;146:1–10.
[38] Zeng X, Ge Y, Shen J, et al. The optimization of channels for a proton exchange membrane fuel cell applying genetic algorithm. Int J Heat Mass Tran 2017;105:81–9.
[39] Cai G, Liang Y, Liu Z, et al. Design and optimization of bio-inspired wave-like channel for a PEM fuel cell applying genetic algorithm. Energy 2020;192:116670.
[40] Huang T, Wang W, Yuan Y, et al. Optimization of high-temperature proton exchange membrane fuel cell flow channel based on genetic algorithm. Energy Rep 2021;7:1374–84.
[41] Zhou Z, Qiu D, Peng L, et al. Channel/rib patterns optimization of a proton exchange membrane fuel cell by combining down-the-channel performance model and genetic algorithm[J]. Int J Heat Mass Tran 2022;183:122235.
[42] Yu Z, Xia L, Xu G, et al. Improvement of the three-dimensional fine-mesh flow field of proton exchange membrane fuel cell (PEMFC) using CFD modeling, artificial neural network and genetic algorithm[J]. Int J Hydrogen Energy 2022;47(82):35038–54.
[43] Wang ZM, Xu C, Wang XY, et al. Numerical investigation of water and temperature distributions in a proton exchange membrane electrolysis cell. Sci China Technol Sci 2021;64(7):1555–66.
[44] Soderberg JN, Co AC, Sirk AHC, et al. Impact of porous electrode properties on the electrochemical transfer coefficient. J Phys Chem B 2006;110(21):10401–10.
[45] Wang XY, Wang ZM, Feng YC, et al. Three-dimensional multiphase modeling of a proton exchange membrane electrolysis cell with a new interdigitated-jet hole flow field [J]. Sci China Technol Sci 2022;65(5):1179–92.
[46] Doubek G, Robalinho E, Cunha EF, et al. Application of CFD techniques in the modelling and simulation of PBI PEMFC. Fuel Cell 2011;11(6):764–74.
[47] Wang L, Guo H, Ye F, et al. Two-dimensional simulation of mass transfer in unitized regenerative fuel cells under operation mode switching. Energies 2016;9(1):47.
[48] Srinivasan S. Fuel cells: from fundamentals to applications. Springer Science & Business media; 2006.
[49] Falcão DS, Pinto A. A review on PEM electrolyzer modelling: guidelines for beginners. J Clean Prod 2020;261:121184.
[50] Meng H, Ruan B. Numerical studies of cold-start phenomena in PEM fuel cells: a review. Int J Energy Res 2011;35(1):2–14.
[51] De Dominici G, Gabriel B. Analytical study of over-voltages in alkaline electrolysis and their parametric dependencies through a multi-physical model. Int J Energy Res 2022;46(3):3295–323.

[52] Chandesris M, Médeau V, Guillet N, et al. Membrane degradation in PEM water electrolyzer: numerical modeling and experimental evidence of the influence of temperature and current density[J]. Int J Hydrogen Energy 2015;40(3):1353–66.
[53] Springer TE, Zawodzinski TA, Gottesfeld S. Polymer electrolyte fuel cell model. J Electrochem Soc 1991;138(8):2334.
[54] Marangio F, Santarelli M, Calì M. Theoretical model and experimental analysis of a high pressure PEM water electrolyser for hydrogen production. Int J Hydrogen Energy 2009;34(3):1143–58.
[55] Du CY, Yin GP, Cheng XQ, et al. Parametric study of a novel cathode catalyst layer in proton exchange membrane fuel cells. J Power Sources 2006;160(1):224–31.
[56] Afshari E, Mosharaf-Dehkordi M, Rajabian H. An investigation of the PEM fuel cells performance with partially restricted cathode flow channels and metal foam as a flow distributor[J]. Energy 2017;118:705–15.
[57] Majasan JO, Cho JIS, Dedigama I, et al. Two-phase flow behaviour and performance of polymer electrolyte membrane electrolysers: electrochemical and optical characterisation. Int J Hydrogen Energy 2018;43(33):15659–72.
[58] Bonanno M, Müller K, Bensmann B, et al. Evaluation of the efficiency of an elevated temperature proton exchange membrane water electrolysis system. J Electrochem Soc 2021;168(9):094504.